

# Detection method for periodic radio emissions from an exoplanet's magnetosphere or a star–planet interaction

C. K. Louis<sup>1,2</sup>, A. Loh<sup>1,2</sup>, P. Zarka<sup>1,2</sup>, L. Lamy<sup>1,2,3</sup>, E. Mauduit<sup>1,2</sup>, J. Girard<sup>1,2</sup>, and Q. Nénon<sup>4</sup>

<sup>1</sup> LIRA, Observatoire de Paris, Université PSL, Sorbonne Université, Université Paris Cité, CY Cergy Paris Université, CNRS, 92190 Meudon, France

e-mail: corentin.louis@obspm.fr

<sup>2</sup> ORN, Observatoire Radioastronomique de Nançay, Observatoire de Paris, CNRS, Univ. PSL, Univ. Orléans, F-18330 Nançay, France

<sup>3</sup> Aix Marseille Université, CNRS, CNES, LAM, Marseille, France

<sup>4</sup> LATMOS, CNRS - Sorbonne Université - CNES, Paris, France

## ABSTRACT

**Context.** The search for exoplanetary or star-planet interaction radio signals is a major challenge, as it is one of the only way of detecting a planetary magnetic field.

**Aims.** The aim of this article is to demonstrate the relevance of using statistical tools to detect periodic radio signals in unevenly spaced observations.

**Methods.** Identification of periodic radio signal is achieved here by a Lomb–Scargle analysis. We first apply the technique on simulated astrophysical observations with controlled simulated noise. This allows for characterizing of spurious detection peaks in the resulting periodograms, as well as identifying peaks due to resonance or beat periods.

**Results.** We then validate this method on a real signal, using  $\sim 1400$  hours of data from observations of Jupiter's radio emissions by the NenuFAR radio telescope over more than six years to detect jovian radio emissions periodicities (auroral and induced by the Galilean moons).

**Conclusions.** We demonstrate with the simulation that the Lomb–Scargle periodogram allows to correctly identify periodic radio signal, even in a diluted signal. On real measurements, it correctly detects the rotation period of the strong signal produced by Jupiter and the synodic period of the emission triggered by the interaction between Jupiter and its Galilean moon Io, but also maybe weaker signal such as the one produced by the interaction between Jupiter and Europa or between Jupiter and Ganymede. It is important to note that secondary peaks in the Lomb–Scargle periodogram will be observed at the synodic and resonance periods between all the detected signal periodicities (i.e. real signals, but also periodicities in the observation). These secondary peaks can then be used to strengthen the detections of weak signals.

**Key words.** Automatic Detection Technics – NenuFAR Radio Telescop – Jupiter Radio Emissions – Exoplanetary Radio Emissions

## 1. Introduction

The best way to detect a magnetic field is to use imaging techniques such as the Zeeman Doppler Imaging (ZDI), which can detect a stellar magnetic field down to 0.8 G (Brown et al. 2022). However, in the case of exoplanetary magnetic fields, they are generally not strong enough to produce a sufficient Zeeman effect on an atom or molecule, i.e. to separate a defined atomic energy level of an atom or molecule into several distinct energy sublevels. Moreover, photon noise severely limits the possibility of detecting this potentially weak polarimetric signal. Finally, the spectrum of the exoplanet is usually combined with that of the star, making it difficult to extract the exoplanet's polarimetric signature. Consequently, ZDI are unable to characterize exoplanetary magnetic fields (for a low limit for low temperatures, see, e.g., Kuzmychov et al. 2017, who present the detection of a magnetic field of 5kG for the brown dwarf LSR J1835+3259 of spectral type M8.5V).

In an other hand, indirect detections of exoplanetary magnetic fields is possible using technics based on planet-modulated chromospheric emission (Cauley et al. 2019) or neutral atomic hydrogen absorption during transit (Ben-Jaffel et al. 2022). An other way to study and characterize exoplanetary magnetic fields

is through the observation of planetary auroral radio emissions. These emissions are produced by the Cyclotron Maser Instability (Treumann 2006), and are well known and studied (remotely and in situ) at Earth, Jupiter and Saturn (Wu & Lee 1979; Le Queau et al. 1984b,a; Wu 1985; Pritchett 1986a; Lamy et al. 2010; Mutel et al. 2010; Kurth et al. 2011; Louarn et al. 2017, 2018; Louis et al. 2023a; Collet et al. 2023, 2024). They occur at or near the fundamental of the local electron cyclotron frequency:

$$f_{ce} = \frac{eB}{2\pi m_e} \quad (1)$$

with  $e$  and  $m_e$  the charge and mass of an electron and  $B$  the local magnetic field amplitude. As the magnetic field amplitude decreases with increasing altitude above the atmosphere, auroral radio emissions span a broad range of frequencies along the magnetic field lines, provided the ratio between the plasma frequency and the cyclotron frequency is less than 0.1. The minimal frequency for the emission is therefore reached at high altitudes (several body radii), while the maximal frequency corresponds to the maximal cyclotron frequency near the planetary surface.

Consequently, detecting these radio emissions provides information about the local magnetic field in situ. For example,

in our Solar System, Jovian auroral radio emissions were first detected (above the ionospheric cutoff at 10 MHz) in 1955 by Burke & Franklin (1955) making Jupiter’s magnetosphere the first to be identified using the radio radiation. Jovian auroral radio emissions extend from a few kilohertz (kilometric range) up to 40 megahertz (decametric range), corresponding to a magnetic field with a maximal amplitude of about 20 G (Connerney et al. 2022).

However, these radio emissions are highly anisotropic. They are produced along the edges of a hollow cone, approximately  $\sim 1 - 2^\circ$  thick, with an opening angle relative to the local magnetic field vector  $\mathbf{B}$  varying from  $\sim 70^\circ$  to  $90^\circ$ , depending on the type of electron distribution function and the emission frequency (Pritchett 1986b; Treumann 2006; Hess et al. 2008). Consequently, the visibility of these emissions strongly depends on the observer’s position in the reference frame of the emitting body (Louis et al. 2021; Lamy et al. 2023b). For instance, in the case of emissions induced by the moon Io (Bigg 1964), a terrestrial observer located approximately in the plane of the equator can only see the emissions when Io is in quadrature (Marques et al. 2017a). Saturn-like auroral radio emissions (fast rotator, sensitive to stellar winds) will be mostly visible for an observer on the morning sector, hence also in quadrature (Lamy 2017; Lamy et al. 2023b, 2008; Kimura et al. 2013; Nakamura et al. 2019). For Earth-like auroral radio emissions (highly sensitive to stellar winds) the maximal chance of detection will be for an observer located in the nightside sector (Waters et al. 2022; Lamy et al. 2023b; Louis et al. 2023b). Finally Jupiter-like auroral radio emissions (strongly magnetized planet and fast rotator, partially sensitive to stellar winds) do not require any preferred position of observation for most of its components (Zarka et al. 2021; Louis et al. 2021; Lamy et al. 2023b; Boudouma et al. 2023).

Another important characteristic of auroral radio emissions is their strong polarization, which is almost 100%. These emissions are produced on the the extraordinary mode (so-called R-X mode), and are therefore circularly or elliptically polarized in the right-hand (RH) sense relative to the magnetic field at the source. The observed polarization thus depends on the magnetic hemisphere: it is RH when the  $(\mathbf{B}, \mathbf{k})$  angle is acute (with  $\mathbf{k}$  the radio wave vector) and LH when the  $(\mathbf{B}, \mathbf{k})$  angle is obtuse.

However, these signal are really weak and sporadic, and only detection attempts have been published so far (Turner et al. 2021, 2023, 2024). To detect these weak astrophysical signals (Zarka et al. 2018), it is crucial to both use prediction tools (e.g., EXPRES, Louis et al. (2019); PALANTIR, Mauduit et al. (2023, 2025); phase prediction<sup>1</sup>, Zhang et al. (2025)) and to accumulate many hours of observations using sensitive radio telescopes (Turner et al. 2019).

With sufficient observation hours over an extended period, it should in principle become possible to search for periodicity in the signal, instead of searching for individual weak and sporadic radio emissions. However, a significant challenge arises from the uneven spacing of these observations over time. Due to the limited observability of the sources (not 24 hours a day) and high observing pressure on giant telescopes such as NenuFAR (Zarka et al. 2020), regular observations are impractical. Consequently, periodicity search techniques capable of handling unevenly spaced observations are required, and the Lomb–Scargle (LS) periodogram such as the one provided by the Astropy python package (Astropy Collaboration et al. 2013, 2018, 2022;

VanderPlas et al. 2012; VanderPlas & Ivezić 2015) is an excellent option for this purpose. The Lomb–Scargle periodogram has for instance proved to be successful to track the double radio period of Saturn’s Kilometric Radiation (e.g., Lamy 2017) or the period of Jovian quasi-periodic bursts (Kimura et al. 2011).

In this paper, we conduct a practical test on real NenuFAR data. To understand how the Lomb–Scargle periodogram performs on NenuFAR data, we first test it on a simulated signal (see Section 2). Initially, we use a sine wave with a known periodicity and random observation gaps. Next, we produce a similar simulation, but this time we control the observation windows and gaps between observations to study the impact of observation regularity on the Lomb–Scargle periodogram, hence mimicking real observing conditions. Finally, we embed the signal in random noise with a normal distribution and study how varying the signal-to-noise ratio affects the detection of the underlying periodic signal.

In Section 3, we apply the Lomb–Scargle periodogram to real observations of Jupiter’s radio emissions acquired over a 6 year long interval with the NenuFAR radio telescope to analyse the periodicities detection.

Finally, in Section 4, we summarize and discuss this study to highlight the constraints and limitations of using this technique for detecting radio emissions by searching for signal periodicity.

## 2. Simulations

In the first simulation (see Figure 1 left), we create a sinusoid signal wave (in blue) of periodicity  $T_{\text{sine}} = 12.90$  hours (Amplitude between -1 and 1) over 5 years (only a few tens of days are shown for the sake of visibility) with a time resolution of 600 seconds. We then randomly keep 2.65% of the signal. By anticipation to the real signal we chose a periodicity of 12.9 hours as it is close to the real physical periodicity we will search for in Section 3. The percentage of kept signal is chosen on the basis of the actual percentage of data actually observed, which will be analysed later in section 3. The corresponding Lomb–Scargle periodogram is shown on the right of Figure 1. The highest peak, by far, in the periodogram is located at 12.9 hours. Confidence levels, based on randomization test, are also shown. Our randomisation test consists of taking the timeserie under consideration, shuffling the values randomly over time and calculating the resulting Lomb–Scargle periodogram. For this test to have sufficient statistical validity, it is repeated 100 times. The confidence levels therefore indicate the percentage of times the highest peak reaches this power value. In the case of this first simulation, all confidence level are obviously close to 0, as there is only signal given as input and that the portion of kept signal is taken fully randomly.

In Figure 2, the same sinusoidal wave is simulated (i.e., with a  $T_{\text{sine}} = 12.9$  h periodicity and a time resolution of 600 seconds), but this time we use more realistic values to select the signals we keep. 2.65% of the signal is also kept, gathered in 125 interval of 8 hours separated by  $N \times 23.93$  hours (with  $N = 1, 2, 3, 4, \dots$ ). These values are chosen on the basis of the real observations values of the target studied in Section 3. The corresponding Lomb–Scargle periodogram is shown on the right of Figure 2. The highest peak is still located at 12.9 hours. But this time, several others peaks are also visible, mainly at 27.99 hours, 8.38 hours and 6.21 hours Figure 3 shows the effect of the windowing on the Lomb–Scargle periodogram. In this Figure, we take the same sinusoid wave than in Figure 2, but we make all values equal to 1 (left panel). In the LS periodogram (right panel)

<sup>1</sup> [https://github.com/zhangxiang-planet/orbital\\_coverage](https://github.com/zhangxiang-planet/orbital_coverage)

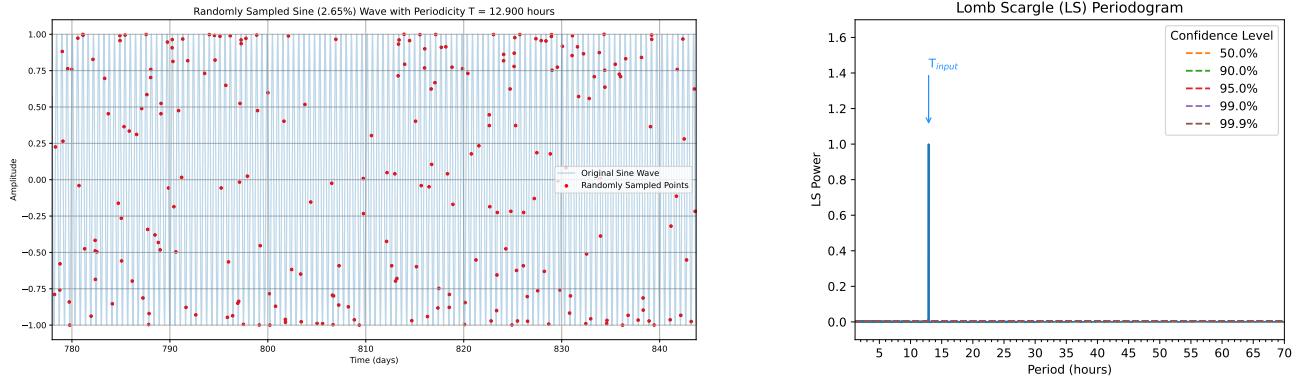


**Fig. 1.** (left) Randomly spaced sinusoidal wave with period  $T_{\text{sine}} = 12.90$  h. Only a few days over the entire 5–year interval are shown, in order to see the sinusoidal signal (right) Corresponding Lomb–Scargle Periodogram. Confidence levels (based on randomization test) are indicated for the Lomb–Scargle periodogram.

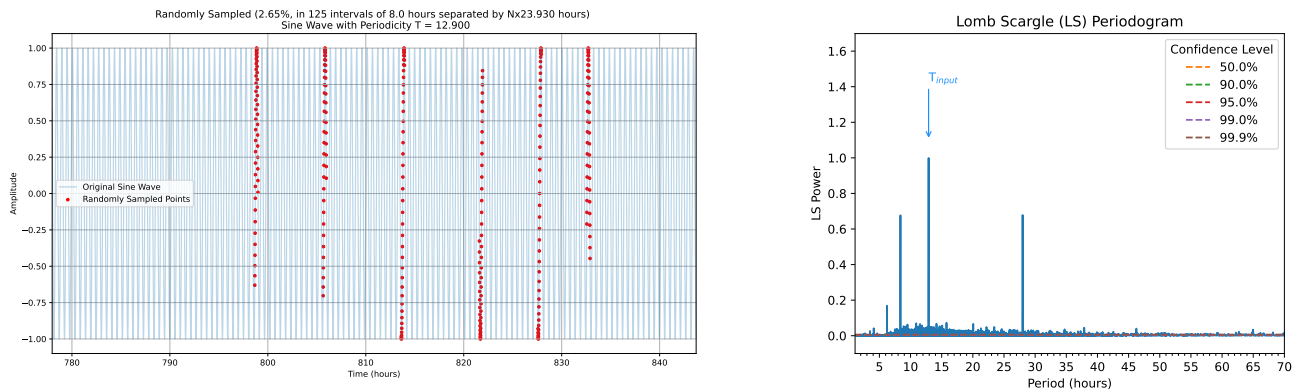


**Fig. 2.** (left) Semi-regularly spaced sinusoidal wave with period  $T_{\text{sine}} = 12.90$  h. The samples are gathered into 125 intervals of 8 hours, spaced by  $N \times 23.93$  hours (with  $N = 1, 2, 3, 4, \dots$ ). (right) Corresponding Lomb–Scargle Periodogram. Confidence levels are also indicated.

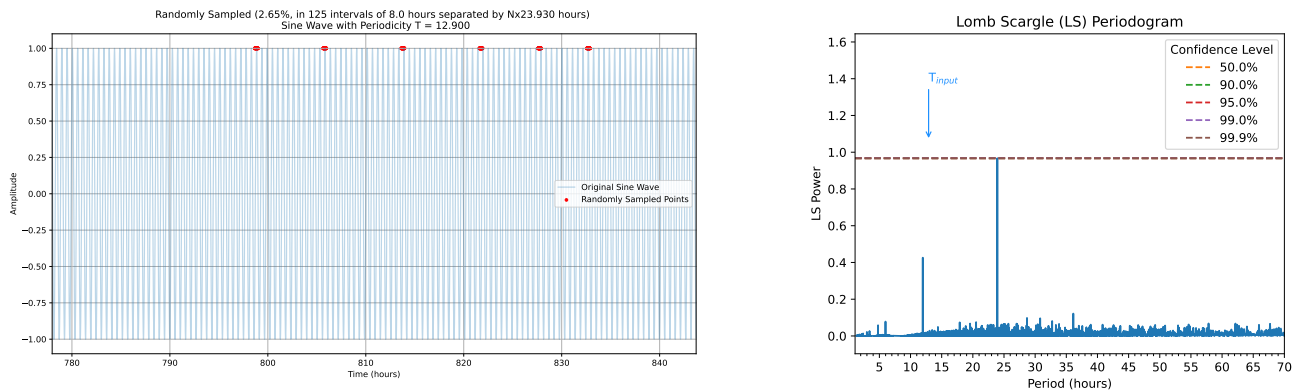


**Fig. 3.** Same as Figure 2, but with all values of the sinusoid at 1, in order to show the effect of the windowing on the Lomb–Scargle periodogram. Confidence levels are also indicated.

the input sinusoidal periodicity is not visible anymore. However, two major peaks are detected at 23.93 hours and 11.99 hours (beat) periods.

To identify the origin of these different peaks, we need to study the possible combinations of resonances between different periodicities. The two major combinations are (i) the synodic (or

$$T_{\text{synodic}} = \frac{T_1 \times T_2}{|T_1 - T_2|} \quad (2)$$

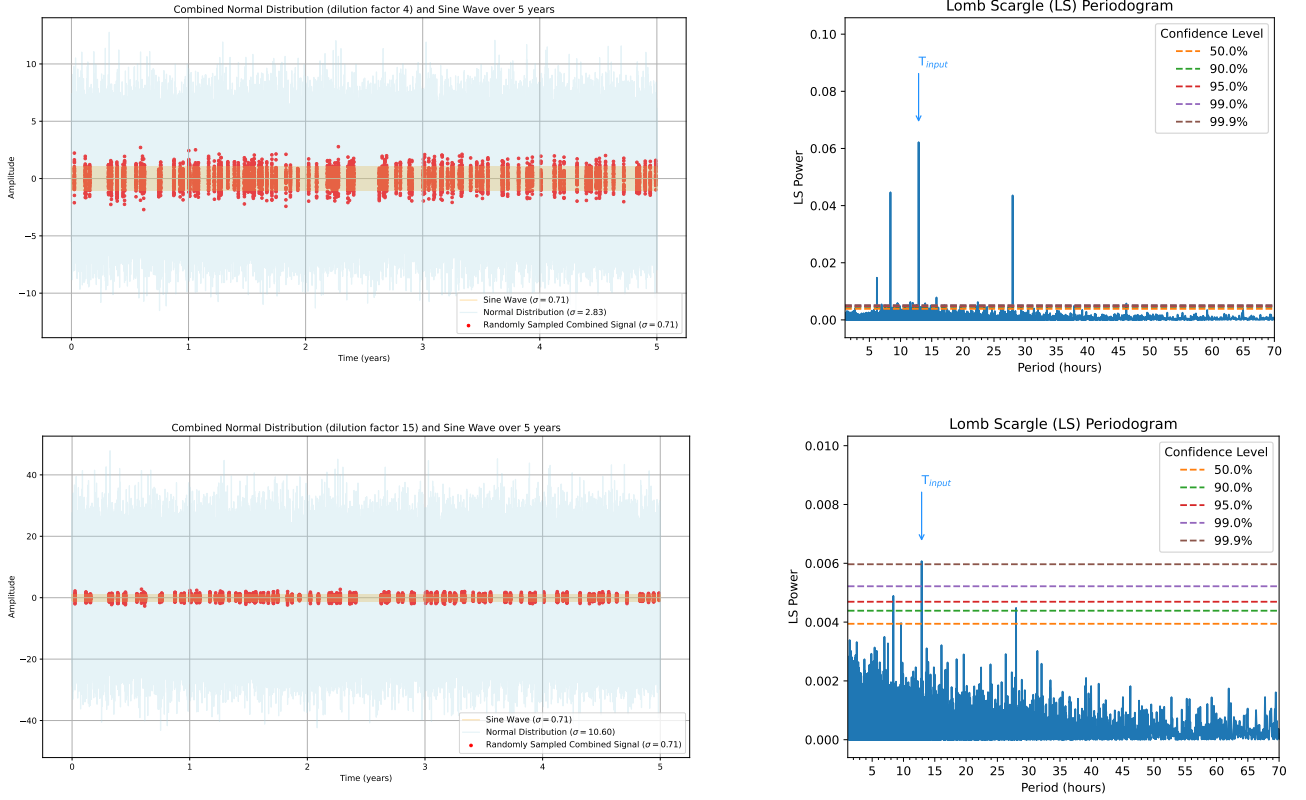


**Fig. 4.** (left panels) Semi-regularly spaced sinusoidal wave with period  $T_{\text{sine}} = 12.90$  h (orange), normal distribution with a standard deviation  $\sigma = K \times \sigma_{\text{sin}}$  (light blue), and combined signal with higher signal to noise ratio (red points). The samples are gathered into 125 intervals of 8 hours, spaced by  $N \times 23.93$  hours. (right panels) Corresponding Lomb–Scargle Periodogram. Top panels are for  $K = 4$  and bottom panels for  $K = 15$ . Confidence levels are also shown in the Lomb–Scargle periodograms.

and (ii) harmonic combination resonance:

$$T_{\text{combination}} = \frac{1}{n \times 1/T_1 + m \times 1/T_2} \quad (3)$$

with  $n, m = 1, 2, 3, 4, \dots$

In our case, we have two fixed periodicities,  $T_{\text{sine}} = 12.9$  h and  $T_{\text{obs}} = 8$  h, while  $T_{\text{gap}} = N \times 23.93$  h can vary with  $N = 1, 2, 3, 4, \dots$ . Therefore, several combinations are possible, including the following synodic periods between:

- $T_{\text{sine}}$  and  $T_{\text{obs}}$ : 21.061 hours
- $T_{\text{obs}}$  and  $N \times T_{\text{gap}}$ :
  - $N = 1$ : 12.02 hours
  - $N = 2$ : 9.61 hours
  - $N = 3$ : 9.00 hours
  - $N = 4$ : 8.73 hours
- $T_{\text{sine}}$  and  $N \times T_{\text{gap}}$ :
  - $N = 1$ : 27.99 hours
  - $N = 2$ : 17.66 hours
  - $N = 3$ : 15.73 hours
  - $N = 4$ : 14.91 hours

and the following harmonic resonances between:

- $T_{\text{sine}}$  and  $T_{\text{obs}}$ : 4.938 hours
- $T_{\text{obs}}$  and  $N \times T_{\text{gap}}$ :
  - $N = 1$ : 5.99 hours
  - $N = 2$ : 4.79 hours
  - $N = 3$ : 3.99 hours

- $N = 4$ : 3.42 hours
- $T_{\text{sine}}$  and  $N \times T_{\text{gap}}$ :
  - $N = 1$ : 8.38 hours
  - $N = 2$ : 6.21 hours
  - $N = 3$ : 4.93 hours
  - $N = 4$ : 4.08 hours

Therefore, the two major peaks that we see in Figure 3 are explained by the periodicity of the gap itself, i.e.,  $T_{\text{gap}} = 23.93$  hours and  $\frac{T_{\text{gap}}}{2} = 11.97$  hours. The two small peaks are them explained by the harmonic resonance between  $T_{\text{obs}} = 8$  h and  $N \times T_{\text{gap}} = N \times 23.93$  h with  $N = 1$  ( $\frac{1}{1/T_{\text{obs}} + 1/T_{\text{gap}}} = 5.99$  hours) and  $N = 2$  ( $\frac{1}{1/T_{\text{obs}} + 2/T_{\text{gap}}} = 4.79$  hours). All these peaks are therefore only due to the windowing of the observations (periodicity of the observations length and interval between 2 consecutive observations). All confidence levels are obviously at the value of the highest peak, since all data points are equal to 1, and shuffling them randomly over the time intervals makes no difference to the Lomb–Scargle analysis.

Concerning the peaks observed in Figure 2, they can be explained by (i) the synodic period between the sinusoidal signal  $T_{\text{sine}} = 12.90$  hours and the periodicity of the gap between each observations  $T_{\text{gap}} = 1 \times 23.93$  h, i.e.  $\frac{T_{\text{sine}} \times T_{\text{gap}}}{|T_{\text{sine}} - T_{\text{gap}}|} = 27.99$  hours, (ii) the harmonic combination between the sinusoidal signal  $T_{\text{sine}} = 12.90$  hours and the periodicity of the gap between each observations  $N \times T_{\text{gap}} = N \times 23.93$  h, with  $N = 1$  ( $\frac{1}{1/T_{\text{sine}} + 1/T_{\text{gap}}} = 8.38$  hours) and  $N = 2$  ( $\frac{1}{1/T_{\text{sine}} + 2/T_{\text{gap}}} = 6.21$  hours).

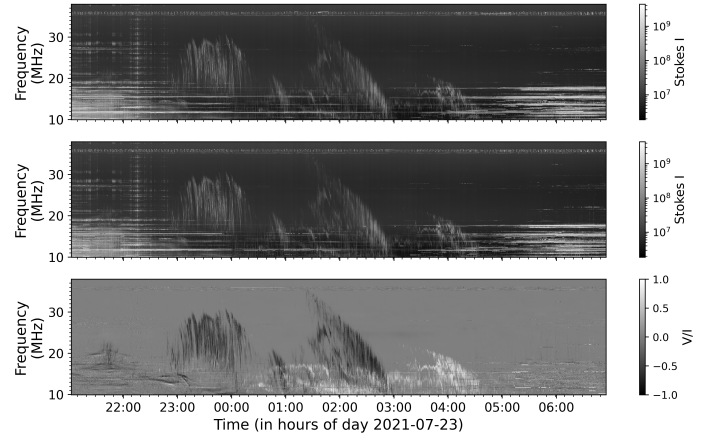
The third simulation (see Figure 4 top-left) is the same simulation than the one in Figure 2, to which we added a normal distribution to dilute the sinusoidal wave. The sinusoidal wave is still centered on 0, with an amplitude between  $-1$  and  $+1$ , with a standard deviation  $\sigma_{\text{sine}} = 0.71$ . The normal distribution we generated has a standard deviation  $\sigma_{\text{normal distribution}} = K \times \sigma_{\text{sine}}$ , with  $K$  the ‘dilution factor’. This distribution is then added to the sinusoidal wave, and we calculate the standard deviation of this combined signal  $\sigma_{\text{combined}}$ . To obtain a combined signal with the same properties as the original signal, in order to decrease its signal to noise ratio, we calculate a conversion factor based on the  $\sigma_{\text{normal distribution}}/\sigma_{\text{sine}}$  ratio and we divide the combined signal by this ratio. We called this new signal the ‘‘corrected combined signal’’. Finally, as for the previous simulations, we keep 2.65% of the signal, gathered in 125 interval of 8 hours separated by  $N \times 23.93$  hours (with  $N = 1, 2, 3, 4, \dots$ ) and a time resolution of 600 seconds.

Figure 4 shows two examples. One with a dilution factor  $K = 4$  (top panels), and one with  $K = 15$  (bottom panels). As one can see (left panels), the standard deviation of the original sinusoidal wave and of the corrected combined signal is the same. However, the Lomb–Scargle periodograms (right panels) are different, even if we are still able to detect the period of the input sine  $T_{\text{sine}} = 12.90$  h in both cases, even if the noise in the Lomb–Scargle has drastically risen, and the value of the peaks drastically decreased. The two others highest peaks are still located at 8.38 hours (harmonic resonance between  $T_{\text{gap}}$  and  $T_{\text{sine}}$ ) and at 27.99 hours (synodic period between  $T_{\text{gap}}$  and  $T_{\text{sine}}$ ). This last Lomb–Scargle periodogram strongly resembles what is observed for real data, as presented in the following section. The confidence levels are located at higher LS power values, confirming that the noise is much more present in that case. The 3 highest peaks, related to  $T_{\text{sine}}$ , are still well above the 90% level, and only the peak at  $T_{\text{sine}}$  is above the 99.9% level.

### 3. Application to real signal: Jupiter observation with NenuFAR

In this section, we analyse real observations of Jupiter’s radio emissions collected using the NenuFAR radio telescope<sup>2</sup> (Zarka et al. 2012). The Jupiter observations consist of time-frequency arrays of the Stokes parameters, which were acquired with the NenuFAR beamforming mode throughout a dedicated Long-Term (LT) Key Program (KP) from 2019 September – 2022 November (Early Science (ES) phase) to 2025 (regular cycles 1 to 5). The number of available Mini-Arrays (MA, sub-groups of 19 antennas) increases over time: up to April 2022, it progressively increases from 51 to 56 MA used; after April 2022, the maximum number of available MA was 78. Note that for maintenance reasons, depending on observations, between 67 and 78 MA were used after April 2022. The observations used a typical  $84 \text{ msec} \times 12 \text{ kHz}$  sampling and were scheduled close to peri-joves of the Juno spacecraft orbiting around Jupiter (Bolton et al. 2017). From cycles 2 to 4, the observations were additionally scheduled to track decametric emissions induced by Io, Europa and Ganymede (Lamy et al. 2023a). It is also worth mentioning that the effective area of NenuFAR antennas, and therefore the final instrumental sensitivity, has regularly increased from 2019 to 2025. Overall, this large NenuFAR/Jupiter dataset consists of 176 independent observations of  $\sim 8$  hours, corresponding to a total exposure of  $\sim 1400$  hours. The interval between the start times of two consecutive observations is  $N \times 23.93$ , with

$N = 1, 2, 3, 4, 5, \dots$ , corresponding to  $N \times 23$  hours, 55 minutes, and 48 seconds –the duration for Jupiter to return to the meridian for a fixed observer on Earth. This periodicity is also very close to the Earth rotation period, i.e. 23 hours, 56 minutes, 4 seconds  $\approx 23.934$  hours. Therefore, these two periodicities will probably be merge in the Lomb–Scargle analysis, and we will only refer to it as  $T_{\text{Day}}$  hereafter.



**Fig. 5.** Typical NenuFAR ‘‘time (UTC) versus frequency (in MHz) spectrogram’’ of Jupiter signal. (Top panel) Stokes I. (Middle panel) Stokes I with RFI mitigation applied (see text). (Bottom panel) Ratio between Stokes  $V$  and Stokes  $I$  showing the degree of Circular Polarization.

An typical observation is displayed in Figure 5. Top panel shows Stokes I parameter and middle panel Stokes I with a preprocessing applied. This preprocessing of the data consists of a time-frequency integration of the data to  $\sim 251 \text{ msec} \times \sim 24 \text{ kHz}$ . During this integration, bad pixels are stored as a weight mask of the same size (nt,nf) as the reduced Stokes I data. Each value of the flag mask is the fraction (0...1) of the good pixels integrated to obtain the corresponding pixel in the reduced data. This weight array is thresholded at 50% (i.e. values  $\leq 0.5$  are set to 0, values  $> 0.5$  are set to 1). Bottom panel displays the degree of circular polarization, defined as the ratio between Stokes  $V$  and Stokes  $I$ , with values ranging between  $-1$  and  $1$ .

In this Figure, Radio Frequency Interferences (RFI) can clearly be seen in the Stokes I data below 20 MHz, before 23:00 UTC and after 04:00 UTC, i.e. at day time. As these RFI are almost not circularly polarized, they are not visible in the  $V/I$  data. In both Stokes I and  $V/I$  ratio, radio emissions are clearly visible between 23:00 and 05:00. These emissions display different degree of circular polarization, providing insight into the polarization characteristics of the emissions and their hemisphere of origin:  $V/I > 0$  corresponds to LH emissions therefore originating from the Southern hemisphere of Jupiter, while  $V/I < 0$  corresponds to RH emissions therefore originating from the Northern hemisphere of Jupiter. Using the Jupiter Probability Tool (Cecconi et al. 2023) we identified these features as Io-induced emissions.

In the following, we will focus on this circular degree of polarization, as RFI and sky background have little or no circular polarization, resulting in a better Signal to Noise Ratio (SNR). We also further process (using the pipeline of Louis et al. 2025a) the observations to a time resolution of 600 seconds, and a frequency resolution of 1 MHz, ranging from 8 MHz to 88 MHz, to further increase the SNR (to access the processed data, please see Louis et al. 2025b). Note here that we have kept the data up

<sup>2</sup> <https://nenufar.obs-nancay.fr>

**Table 1.** Possible fundamental, synodic and harmonic periods that could be expected due to the rotation periods of Jupiter and its moons, and the day/ observation periodicity

	$T_{\text{Jupiter}}$	$T_{\text{Day}}$	$T_{\text{Io}}$	$T_{\text{Europa}}$	$T_{\text{Ganymede}}$
Period	9.93	23.93	42.46	85.23	171.71
Half period	4.97	11.97	21.23	42.62	42.93
Synodic periods					
$T_{\text{Jupiter}}$	N.A.	16.97	12.96	11.24	10.54
$T_{\text{Day}}$	16.97	N.A.	54.83	33.27	27.8
$T_{\text{Io}}$	12.96	54.83	N.A.	84.61	56.41
$T_{\text{Europa}}$	11.24	33.27	84.61	N.A.	169.23
$T_{\text{Ganymede}}$	10.54	27.81	56.41	169.23	N.A.
Harmonic periods					
$T_{\text{Jupiter}}$	N.A.	7.02	8.048	8.89	9.39
$T_{\text{Day}}$	7.02	N.A.	15.31	18.68	21.00
$T_{\text{Io}}$	8.048	15.31	N.A.	28.34	34.04
$T_{\text{Europa}}$	8.89	18.68	28.34	N.A.	56.96
$T_{\text{Ganymede}}$	9.39	21.00	34.04	56.96	N.A.

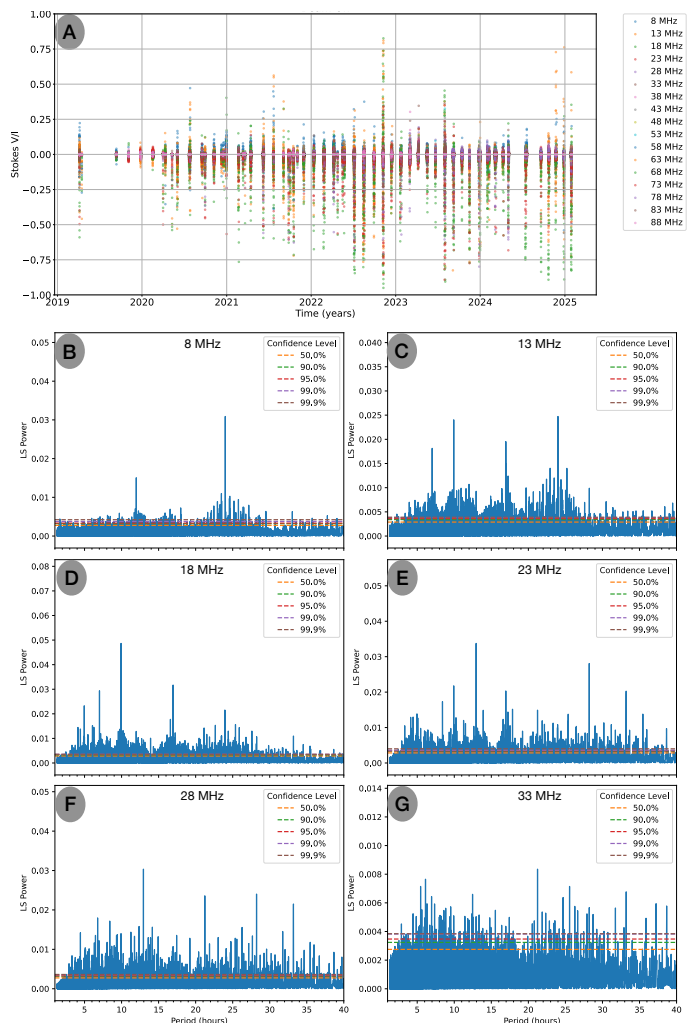
to 88 MHz, since it was acquired up to this frequency from April 2023, with a view to observing synchrotron radiation. However, the circular polarisation expected for this radiation is weak to non-detectable in this frequency range (Girard et al. 2016), as Jupiter’s radiation belt system is not resolved with NenuFAR resolution, which may lead to circular polarisation smearing. So hereafter we will only analyse circular polarisation data up to 40 MHz, the upper limit of auroral radiation.

Table 3 lists the possible fundamental periods for Jupiter  $T_{\text{Jupiter}}$ , Io  $T_{\text{Io}}$ , Europa  $T_{\text{Europa}}$  and Ganymede  $T_{\text{Ganymede}}$ , and the day/observation periodicity  $T_{\text{Day}}$ , and the different combination between them, i.e. synodic and harmonic periods, that can be expected to be found in the Lomb–Scargle periodograms that follow.

Figure 6A shows the circular degree of polarization (Stokes V/I) measurements for 5 MHz-frequency bands. Figure 6B–G show the Lomb–Scargle periodograms for 5 MHz-frequency bands in the range [8–38] MHz. Figure 7 is a summary in 2D (observed frequency vs. Lomb–Scargle periodicities) and displays the SNR of the Lomb–Scargle power. The noise is calculated at each frequency band as the standard deviation of the Lomb–Scargle periodogram. The SNR is intentionally thresholded to remove the noise (see Figs. 6B–G).

Depending on the frequency, different peaks are visible. First, peaks are detected at 9.93 hours between  $\sim 13$ –25 MHz and at 4.97 hours between 19–24 MHz, which corresponds to the fundamental of Jupiter rotation period  $T_{\text{J}}$  and half Jupiter rotation period  $T_{\text{J}/2}$ . Two others peaks are linked to Io: one detected at 12.96 hours between  $\sim 23$ –33 MHz, which corresponds to the synodic period between Jupiter and its Galilean moon Io  $T_{\text{syn IJ}}$ , and a second one at 21.23 hours between 26 – 33 MHz corresponding to the Io half keplerian rotational period  $T_{\text{Io}/2}$ , implying that the LS analysis detects radio emissions related to Jupiter itself and induced by Io (at Io keplerian revolution or Io-Jupiter synodic periods). Peaks related to Jupiter are seen at lower frequencies than the ones related to Io, which is due to the topology of the Jovian magnetic fields.

Below 21 MHz, an other strong peak is detected at  $\sim 23.93$  hours. This corresponds to both the period for Jupiter to be visible in the sky and the Earth rotation period  $T_{\text{day}}$ . The former periodicity only affects the jovian auroral radio emissions (usually seen  $< 25$  MHz, due to Jupiter magnetic field topology



**Fig. 6.** (left panel) Real Data from NenuFAR observations. The color corresponds to different frequency ranges of 5 MHz. (right panels) Corresponding Lomb–Scargle Periodograms for seven frequency ranges averaged on 5 MHz bandwidth ([8–13] MHz, [13–18] MHz, [18–23] MHz, [23–28] MHz, [28–33] MHz, [33–38] MHz, from left to right and from top to bottom).

connected to the magnetic field lines producing these emissions) as they can be observed almost each time Jupiter is visible in the sky, while Io-induced emission are visible only if Io is in quadrature. The latter affects the background radio signal visibility, most probably the RFI still visible in the V/I data, which are also only visible  $\leq 20$  MHz (see Figure 5), since this periodicity is only detected at low frequency. An harmonic of this peak is also visible at  $T_{\text{D}/2}$ .

Four other peaks are also visible. Two above 23 MHz are related to Io’s periods (keplerian and synodic with Jupiter): (i) at 28.27 hours between 23–33 MHz corresponding to the synodic period  $T_{\text{syn D-IJ}}$  between the  $T_{\text{syn IJ}}$  and  $T_{\text{D}}$  periodicities; (ii) at 33.27 hours between 24–32 MHz corresponding to the synodic period  $T_{\text{syn I/2-IJ}}$  between the Io half keplerian revolution period  $T_{\text{Io}/2}$  and the  $T_{\text{syn IJ}}$  period. Two are contained in the range 13–25 MHz and are related to Jupiter’s period: (i) the harmonic period  $T_{\text{harm JD}}$  between the Jupiter  $T_{\text{J}}$  and the day  $T_{\text{D}}$  periodicities at 7.02 hours between 13–23 MHz and (ii) the synodic period  $T_{\text{syn DJ}}$  between the Jupiter  $T_{\text{J}}$  and the day  $T_{\text{D}}$  periodicities at 16.97 hours between 13–25 MHz.

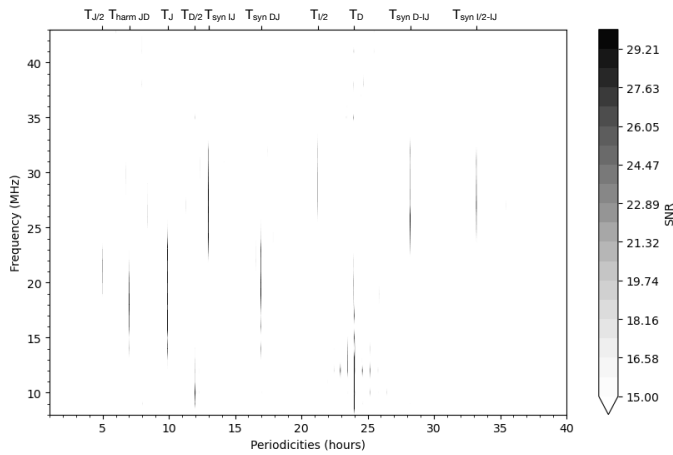


**Fig. 7.** Signal to Noise ratio of the 2D Lomb–Scargle Periodogram. Y-axis represents the observed frequencies (from 8 to 43 MHz), X-axis represents the Lomb–Scargle Periodicities. Periodicities of interest are indicated above the top y-axis.

Interestingly, the peaks at  $T_{harm\ DJ}$ ,  $T_{syn\ DJ}$ ,  $T_{syn\ D-IJ}$  and  $T_{syn\ I/2-IJ}$  each combined individual Lomb–Scargle power at two different frequencies, therefore strengthening the detection of periodic signals at  $T_{syn\ IJ}$ ,  $T_{1/2}$  and  $T_J$ , providing robust evidence for these periodicities.

Some other potential periodicities we could have expected would have been linked to two others Galilean moons, mainly Europa and Ganymede, as they also induced radio emissions in the decametric range (Louis et al. 2017, 2023a; Zarka et al. 2018; Jácóme et al. 2022). As for Io, the expected periodicity would have been at the synodic period with Jupiter, i.e.,  $T_{syn\ Europa-Jupiter} = 11.24$  hours and  $T_{syn\ Ganymede-Jupiter} = 10.54$  hours. No major peaks are visible at these periodicities even if a small peak is observed at  $T_{syn\ Europa-Jupiter}$  (LS Power =  $\sim 0.014$ ) in Figures 6E-F. This is not a surprise, as almost all radio emission detected in the NenuFAR Jupiter observation is known to be associated with the Io–Jupiter interaction or to Jupiter itself. We will come back on periodic signal at  $T_{syn\ Europa-Jupiter}$  in the following paragraphs.

Based on the detected peaks at specific periodicities, we aim to constrain when the signals contributing to the LS power were actually observed. The LS periodogram, initially calculated over the data acquired during the over 6-year interval, raises the question of whether similar analyses could be performed over shorter time spans. To address this, Figure 8 displays the SNR of the LS periodogram calculated over time for different frequency ranges using a sliding window approach. Each window spans 500 days and slides every 2 days. Note that we studied the effect of the window size and slide. After several tests, we have determined that window size of 500 days and a slide of the window of  $\sim 1\%$  of the window size gives the best results. A too small windows (e.g. 100 days) induces an large increase of noise.

In this Figure, we zoom-in over the 4–20 hours LS periodicities as it highlights most of the periodicities of interest, including  $T_{syn\ D-IJ}$ ,  $T_{syn\ I-IJ}$ ,  $T_{day/2}$ ,  $T_{syn\ E-IJ}$  (for Europa–Jupiter),  $T_{syn\ G-IJ}$  (for Ganymede–Jupiter),  $T_{Jupiter}$ ,  $T_{harm\ D-IJ}$ ,  $T_{Jupiter/2}$ , presented from top to bottom in each panel.

For the [8–18[ MHz range (Figure 8A), a notable large peak is centered at  $T_{day/2} = 11.97$  hours, both due to the Earth rotation period but also the return of Jupiter in the sky.

Some peaks are closely aligned with Jupiter periodicities, at  $T_{Jupiter}$ ,  $T_{Jupiter/2}$  or at  $T_{syn\ D-IJ}$  and  $T_{harm\ D-IJ}$  the synodic and harmonic period between the day and Jupiter periodicities, or Io–Jupiter synodic period  $T_{syn\ I-IJ}$  (e.g. Figures 8D-F). Interestingly, enhancement of the SNR of the LS power is visible at  $T_{syn\ E-IJ}$ , the synodic period between Jupiter and the Galilean moon Europa, in the [13–18[ MHz frequency range during 2021 (panel 8B) and in the [23–28[ frequency range from mid-cycle 2 to mid-cycle 3 (panel 8D) and at  $T_{syn\ G-IJ}$ , the synodic period between Jupiter and the Galilean moon Ganymede, in the [13–18[ MHz frequency range mainly during Cycle 1 and also time to time during the ES phase (panel 8B).

These results emphasize the potential of LS periodograms, calculated over shorter time spans, to reveal temporal variations in signal periodicities and to identify specific intervals of enhanced observational significance.

## 4. Summary and Discussions

In this article, we analyse and demonstrate how the use of Lomb–Scargle is affected by a non-continuous signal that is more or less regular in time, and more or less diluted in noise. We analyse the different peaks in the periodogram and how they can be associated with real signals.

First, we simulated a sinusoidal signal with a periodicity of  $T = 12.9$  hours, an amplitude between  $-1$  and  $1$ , spanning 5 years. We randomly retained only 2.65% of the data points. When we applied the Lomb–Scargle periodogram, the highest peak was clearly located at 12.9 hours, corresponding to the input signal’s periodicity.

In the second simulation, we grouped the retained data into 125 intervals, each lasting 8 hours, separated by  $N = 23.93$  hours ( $N = 1, 2, 3, \dots$ ). The Lomb–Scargle periodogram still showed the highest peak at 12.9 hours, but additional peaks appeared with significant power at periodicities such as 27.8 hours, 8.4 hours, and 6.2 hours. These correspond to the synodic period or harmonic combinations of the input signal’s periodicity and the interval between observations.

In the third simulation, we introduced noise by adding a normal distribution to dilute the signal. This increased the noise in the Lomb–Scargle periodogram, causing a drastic decrease in the normalized peak power. The periodogram started resembling those of real observed signals. Despite this, with a dilution factor of up to 15, the input signal’s periodicity remained detectable, standing out above the noise with a confidence level above 95%. Additionally, two other peaks related to the synodic period and harmonic resonance between the input signal and the observation gap were observed. Even with a diluted signal, the three main peaks retained their link to the input signal, strengthening the detection.

We then applied the Lomb–Scargle periodogram to real observations of the circular degree of polarization of Jupiter’s radio emissions, collected with the NenuFAR radio telescope. Depending on the analysis method—either over the entire 6-year interval or using a sliding window of 500 days with a 2-day step—and the observed frequency range, we detected different peaks. At low frequencies, the highest peak was found at 23.93 hours, corresponding to both Earth’s rotation and the return of Jupiter in the sky. A smaller peak was also detected at half this period. These peaks are only visible at low frequencies for two probable reasons: (i) there are still some RFI present in the V/I data, and these RFI are only visible below 20 MHz during day; (ii) only the jovian auroral radio emissions (usually seen  $< 25$  MHz) affect these periodicities, as they can be observed

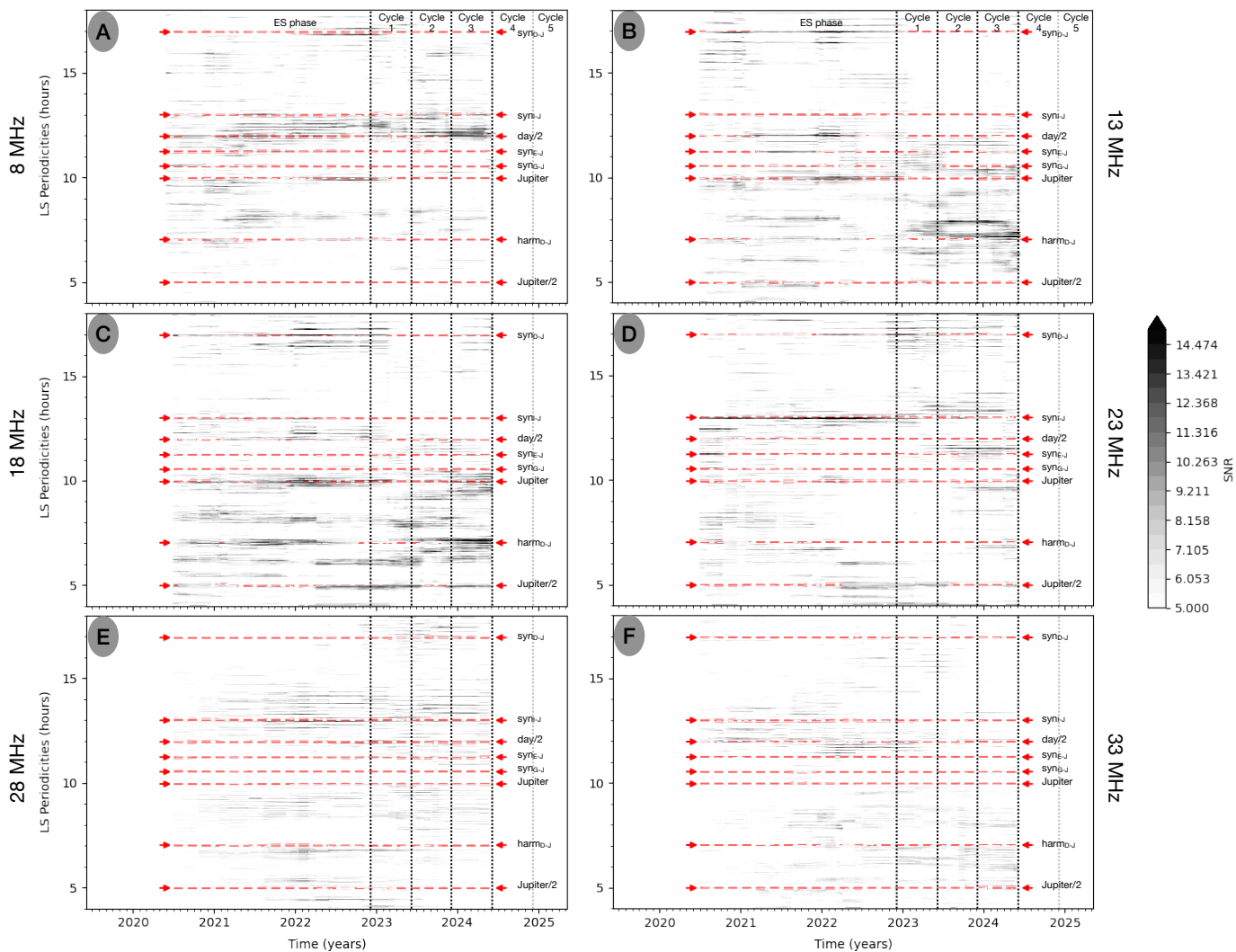


**Fig. 8.** Signal to Noise ratio of 2D Lomb–Scargle Periodograms for six different 5-MHz frequency intervals ([8-13[ MHz, [13-18[ MHz, [18-23[ MHz, [23-28[ MHz, [28-33[ MHz and [33-38[ MHz). In each panel, Y-axis represents the Lomb–Scargle Periodicities, X-axis represents the calendar time (in Year). The Lomb–Scargle Periodograms are calculated over a 500 days window sliding 2 days. The mean time is taken for each window, and the corresponding SNR of the LS periodogram is displayed as the grey color shade. The colour bar, thresholded to remove background noise from the periodograms, is the same for all panels. The different red dashed lines give (from top to bottom) the following periodicities:  $T_{\text{syn D-J}}$ ,  $T_{\text{syn I-J}}$ ,  $T_{\text{day/2}}$ ,  $T_{\text{syn E-J}}$  (for Europa–Jupiter),  $T_{\text{syn G-J}}$  (for Ganymede–Jupiter),  $T_{\text{Jupiter}}$ ,  $T_{\text{harm D-J}}$ ,  $T_{\text{Jupiter/2}}$ . The vertical dotted line indicate the NenuFAR observing phase, from Early Science to Cycle 5.

each time Jupiter is visible in the sky, while Io-induced emission are visible only if Io is in quadrature. Four peaks were detected associated with Jupiter’s full and half rotation periods, the synodic period between Jupiter and its moon Io, and half of Io’s Keplerian orbital period. Four additional peaks linked to Jupiter or Io-induced emissions were detected, at both the synodic and harmonic periods between Jupiter and Earth’s day length, between the day and the synodic period between Jupiter and its moon Io, and between half of Io’s Keplerian orbital period and the synodic period between Jupiter and its moon Io.

For the sake of completeness, we also wanted to test this technique on a longer and, above all, pre-catalogued dataset (see Appendix A). To this end, we performed the Lomb–Scargle analysis of the Nançay Decameter Array (NDA) data using (Marques et al. 2017a) catalog, which separates Io-induced from non-Io-induced emissions. Figure A.1 (top panel) shows a 2D periodogram of all the catalogued NDA data. This periodogram

shows, like the one in Figure 7, SNR enhancements at typical periods ( $T_{\text{Jupiter}}$ ,  $T_{\text{syn I/J}}$ ,  $T_{\text{Day}}$ ,  $T_{\text{Day/2}}$ , and synodic and harmonic intervals between these different periodicities), while showing stronger SNR and peaks at many other beat and resonance frequencies that we won’t describe here in detail. However, this LS analysis of such a large dataset (30 years of data with 8 hours daily observations) shows a kind of upper limit to what a Lomb–Scargle analysis can give. Finally, middle and bottom panels of A.1 show LS periodograms of Io and non-Io data, respectively. Comparing them confirms what we described above, i.e. that non-Io emissions (and therefore mainly Jupiter) are only observed below  $\sim 25$  MHz, and that the peaks at  $T_{\text{day}}$  and  $T_{\text{day/2}}$  is mainly due to the return of the auroral Jupiter radio emissions (i.e. non-Io induced) in the observer’s sky, and not much by the Earth rotation period (i.e. the RFI).

Other peaks appeared from the NenuFAR V/I data once we displayed the SNR of the LS over time. Depending on the time



of year enhancement were seen at the synodic period between Jupiter and its moon Europa and at the synodic period between Jupiter and its moon Ganymede. Even if we know that emissions induced by these two moons exist (Louis et al. 2017; Zarka et al. 2017, 2018; Jácóme et al. 2022; Louis et al. 2023a), we might be allowed to doubt their detection here, given that a 1:2:4 resonance exists between Io, Europa and Ganymede. Indeed, there is no filtering or reorganization of the data before applying the LS analysis. Thus, Io’s emissions could disrupt the LS analysis, and their 1-in-2 or 1-in-4 detection could give power to the LS Jupiter-Europa or Jupiter-Ganymede synodic period. However, looking at panel 8B, the SNR increase at the synodic periods of Europa and Ganymede is not observed at the same time, and little to no signal is detected at the synodic period of Io at these times, reinforcing their detection.

These results demonstrate that the Lomb–Scargle periodogram is a powerful tool for detecting periodic radio emissions in unevenly sampled data. It not only identifies strong signals, such as Jupiter’s auroral radio emissions and Io-induced emissions, but also detects weaker signals, such as those linked to Europa or Ganymede.

At first glance, one might think that regular gaps in observation would weaken the analysis by introducing spurious periodic signals. However, as shown in our simulations, regular observation intervals do not produce peaks in the Lomb–Scargle periodogram at those intervals. Instead, they create peaks at resonance or beat periods with the actual signal, which can be used to reinforce detections. Simulations with diluted signals further illustrate that periodicities can be detected even at low signal-to-noise ratios.

Concerning the synchrotron radiation, the instrument resolution needs to be at least half the diameter of Jupiter to resolve both East and West components of the radiation belts. Upcoming SKA-low stations (Dewdney et al. 2022) might bring the necessary baseline to resolve this emission at low frequencies (down to 50 MHz).

In our observations of Jupiter, data were often collected when Io-induced radio emissions were expected. While one might think this biases the results, this approach is consistent with our simulations (where the signal was always present) and parallels current efforts in exoplanet studies, where observations are timed for maximum likelihood of detecting signals, such as during quadrature phases with exoplanets.

This technique will be applied to search for exoplanetary or star-planet interaction signals in NenuFAR radio telescope data.

**Acknowledgements.** C.L., A.L., P.Z., L.L. acknowledge funding from the ERC under the European Union’s Horizon 2020 research and innovation program (grant agreement N° 101020459—Exoradio, doi: 10.3030/101020459). The French authors acknowledge support from CNES and from CNRS/INSU programs of Planetology (ATNP) and Heliophysics (ATST). The NenuFAR data are accessible on demand to the PIs of key projects. The NDA dataset are available at Lamy et al. (2021) and the catalogue at Marques et al. (2017b). Finally, C.L. would like to thank Q. Duchene and J. Morin for their help on getting information on ZDI and the detection limits, and E. Berriot for preliminary discussions on comparisons between periodicities detection techniques.

## Data Availability Statement

Pre-processed data from the NenuFAR Key Project 07 observations of Jupiter used in this article can be accessed at <https://doi.org/10.25935/7a1s-rf17> (Louis et al. 2025b). The pipeline used to create this dataset can be accessed at <https://doi.org/10.5281/zenodo.15065695> (Louis et al. 2025a).

## References

- Astropy Collaboration, Price-Whelan, A. M., Lim, P. L., et al. 2022, *ApJ*, 935, 167
- Astropy Collaboration, Price-Whelan, A. M., Sipőcz, B. M., et al. 2018, *AJ*, 156, 123
- Astropy Collaboration, Robitaille, T. P., Tollerud, E. J., et al. 2013, *A&A*, 558, A33
- Ben-Jaffel, L., Ballester, G. E., García Muñoz, A., et al. 2022, *Nature Astronomy*, 6, 141
- Bigg, E. K. 1964, *Nature*, 203, 1008
- Bolton, S. J., Lunine, J., Stevenson, D., et al. 2017, *Space Sci. Rev.*, 213, 5
- Boudouma, A., Zarka, P., Magalhães, F. P., et al. 2023, in *Planetary, Solar and Heliospheric Radio Emissions IX*, ed. C. K. Louis, C. M. Jackman, G. Fischer, A. H. Sulaiman, & P. Zucca, 103094
- Brown, E. L., Jeffers, S. V., Marsden, S. C., et al. 2022, *MNRAS*, 514, 4300
- Burke, B. F. & Franklin, K. L. 1955, *Journal of Geophysical Research*, 60, 213
- Cauley, P. W., Shkolnik, E. L., Llama, J., & Lanza, A. F. 2019, *Nature Astronomy*, 3, 1128
- Cecconi, B., Aicardi, S., & Lamy, L. 2023, *Frontiers in Astronomy and Space Sciences*, 10
- Collet, B., Lamy, L., Louis, C. K., et al. 2024, *Journal of Geophysical Research (Space Physics)*, 129, e2024JA032422
- Collet, B., Lamy, L., Louis, C. K., et al. 2023, in *Planetary, Solar and Heliospheric Radio Emissions IX*, ed. C. K. Louis, C. M. Jackman, G. Fischer, A. H. Sulaiman, & P. Zucca (Dublin Institute for Advanced Studies and Trinity College Dublin)
- Connerney, J. E. P., Timmins, S., Oliverson, R. J., et al. 2022, *Journal of Geophysical Research (Planets)*, 127, e07055
- Dewdney, P., Labate, M. G., Swart, G., et al. 2022, *SKA: Design Baseline Description, Revision 2, Technical Report SKA-TEL-SKO-0001075, Square Kilometre Array (SKA)*
- Girard, J. N., Zarka, P., Tasse, C., et al. 2016, *A&A*, 587, A3
- Hess, S., Cecconi, B., & Zarka, P. 2008, *Geophysical Research Letters*, 35, L13107
- Jácóme, H. R. P., Marques, M. S., Zarka, P., et al. 2022, *Astronomy & Astrophysics*, 665, A67
- Kimura, T., Lamy, L., Tao, C., et al. 2013, *Journal of Geophysical Research (Space Physics)*, 118, 7019
- Kimura, T., Tsuchiya, F., Misawa, H., et al. 2011, *Journal of Geophysical Research (Space Physics)*, 116, A03204
- Kurth, W. S., Gurnett, D. A., Menietti, J. D., et al. 2011, in *Planetary, Solar and Heliospheric Radio Emissions (PRE VII)*, ed. H. O. Rucker, W. S. Kurth, P. Louarn, & G. Fischer, 75–85
- Kuzmychov, O., Berdyugina, S. V., & Harrington, D. M. 2017, *ApJ*, 847, 60
- Lamy, L. 2017, in *Planetary Radio Emissions VIII*, ed. G. Fischer, G. Mann, M. Panchenko, & P. Zarka, 171–190
- Lamy, L., Duchêne, A., Mauduit, E., et al. 2023a, in *Planetary, Solar and Heliospheric Radio Emissions IX*, ed. C. K. Louis, C. M. Jackman, G. Fischer, A. H. Sulaiman, & P. Zucca, 103097
- Lamy, L., Le Gall, A., Cecconi, B., et al. 2021, *Nançay Decameter Array (NDA) Jupiter Routine observation data collection (Version 1.7) [Data set]*
- Lamy, L., Schippers, P., Zarka, P., et al. 2010, *Geophys. Res. Lett.*, 37, L12104
- Lamy, L., Waters, J. E., & Louis, C. K. 2023b, in *Planetary, Solar and Heliospheric Radio Emissions IX*, ed. C. K. Louis, C. M. Jackman, G. Fischer, A. H. Sulaiman, & P. Zucca, 103091
- Lamy, L., Zarka, P., Cecconi, B., et al. 2008, *Journal of Geophysical Research (Space Physics)*, 113, A07201
- Le Queue, D., Pellat, R., & Roux, A. 1984a, *Physics of Fluids*, 27, 247
- Le Queue, D., Pellat, R., & Roux, A. 1984b, *Journal of Geophysical Research*, 89, 2831
- Louarn, P., Allegrini, F., McComas, D. J., et al. 2017, *Geophysical Research Letters*, 44, 4439
- Louarn, P., Allegrini, F., McComas, D. J., et al. 2018, *Geophysical Research Letters*, 45, 9408
- Louis, C. K., Hess, S. L. G., Cecconi, B., et al. 2019, *Astronomy & Astrophysics*, 627, A30
- Louis, C. K., Lamy, L., Zarka, P., Cecconi, B., & Hess, S. L. G. 2017, *Journal of Geophysical Research (Space Physics)*, 122, 9228
- Louis, C. K., Loh, A., Zarka, P., et al. 2025b, *Pre-processed data from the NenuFAR Key Project 07 observations of Jupiter (Version 1.0) [Data set]*
- Louis, C. K., Loh, A., Zarka, P., Mauduit, E., & Girard, J. N. 2025a, *A Pipeline to process NenuFAR beamformed data and calculate Lomb-Scargle Periodograms*
- Louis, C. K., Louarn, P., Collet, B., et al. 2023a, *Journal of Geophysical Research (Space Physics)*, 128, e2023JA031985
- Louis, C. K., Smith, K. D., Jackman, C. M., et al. 2023b, in *Planetary, Solar and Heliospheric Radio Emissions IX*, ed. C. K. Louis, C. M. Jackman, G. Fischer, A. H. Sulaiman, & P. Zucca, 103088

- Louis, C. K., Zarka, P., Dabidin, K., et al. 2021, *Journal of Geophysical Research (Space Physics)*, 126, e29435
- Marques, M., Zarka, P., Echer, E., et al. 2017b, *Jupiter decametric radio emissions over 26 years*
- Marques, M. S., Zarka, P., Echer, E., et al. 2017a, *Astronomy & Astrophysics*, 604, A17
- Mauduit, E., Duchêne, Q., Griessmeier, J.-M., & Zarka, P. 2025, submitted to *Astronomy & Astrophysics*
- Mauduit, E., Grießmeier, J. M., Zarka, P., & Turner, J. D. 2023, in *Planetary, Solar and Heliospheric Radio Emissions IX*, ed. C. K. Louis, C. M. Jackman, G. Fischer, A. H. Sulaiman, & P. Zucca, 103092
- Mutel, R. L., Menietti, J. D., Gurnett, D. A., et al. 2010, *Geophys. Res. Lett.*, 37, L19105
- Nakamura, Y., Kasaba, Y., Kimura, T., et al. 2019, *Planetary and Space Science*, 178, 104711
- Pritchett, P. L. 1986a, *Journal of Geophysical Research*, 91, 13569
- Pritchett, P. L. 1986b, *Physics of Fluids*, 29, 2919
- Treumann, R. A. 2006, *Astronomy & Astrophysics*, 13, 229
- Turner, J. D., Grießmeier, J.-M., Zarka, P., & Vasylieva, I. 2019, *A&A*, 624, A40
- Turner, J. D., Grießmeier, J.-M., Zarka, P., Zhang, X., & Mauduit, E. 2024, *A&A*, 688, A66
- Turner, J. D., Zarka, P., Grießmeier, J.-M., et al. 2021, *Astronomy & Astrophysics*, 645, A59
- Turner, J. D., Zarka, P., Grießmeier, J. M., et al. 2023, in *Planetary, Solar and Heliospheric Radio Emissions IX*, ed. C. K. Louis, C. M. Jackman, G. Fischer, A. H. Sulaiman, & P. Zucca, 04048
- VanderPlas, J., Connolly, A. J., Ivezic, Z., & Gray, A. 2012, in *Proceedings of Conference on Intelligent Data Understanding (CIDU)*, 47–54
- VanderPlas, J. T. & Ivezić, Ž. 2015, *ApJ*, 812, 18
- Waters, J. E., Jackman, C. M., Whiter, D. K., et al. 2022, *Journal of Geophysical Research (Space Physics)*, 127, e30449
- Wu, C. S. 1985, *Space Science Reviews*, 41, 215
- Wu, C. S. & Lee, L. C. 1979, *Astrophysical Journal*, 230, 621
- Zarka, P., Denis, L., Tagger, M., et al. 2020, in *URSI General Assembly and Scientific Symposium (URSI GASS)*
- Zarka, P., Girard, J. N., Tagger, M., & Denis, L. 2012, in *SF2A-2012: Proceedings of the Annual meeting of the French Society of Astronomy and Astrophysics*, ed. S. Boissier, P. de Laverny, N. Nardetto, R. Samadi, D. Valls-Gabaud, & H. Wozniak, 687–694
- Zarka, P., Magalhães, F. P., Marques, M. S., et al. 2021, *Journal of Geophysical Research (Space Physics)*, 126, e29780
- Zarka, P., Marques, M. S., Louis, C., et al. 2017, in *Planetary Radio Emissions VIII*, ed. G. Fischer, G. Mann, M. Panchenko, & P. Zarka, 45–58
- Zarka, P., Marques, M. S., Louis, C., et al. 2018, *Astronomy & Astrophysics*, 618, A84
- Zhang, X., Zarka, P., Girard, J., et al. 2025, submitted to *Astronomy & Astrophysics*

## Appendix A: Lomb–Scargle Analysis of the Marques et al. (2017a) Nançay Decameter Array Catalog

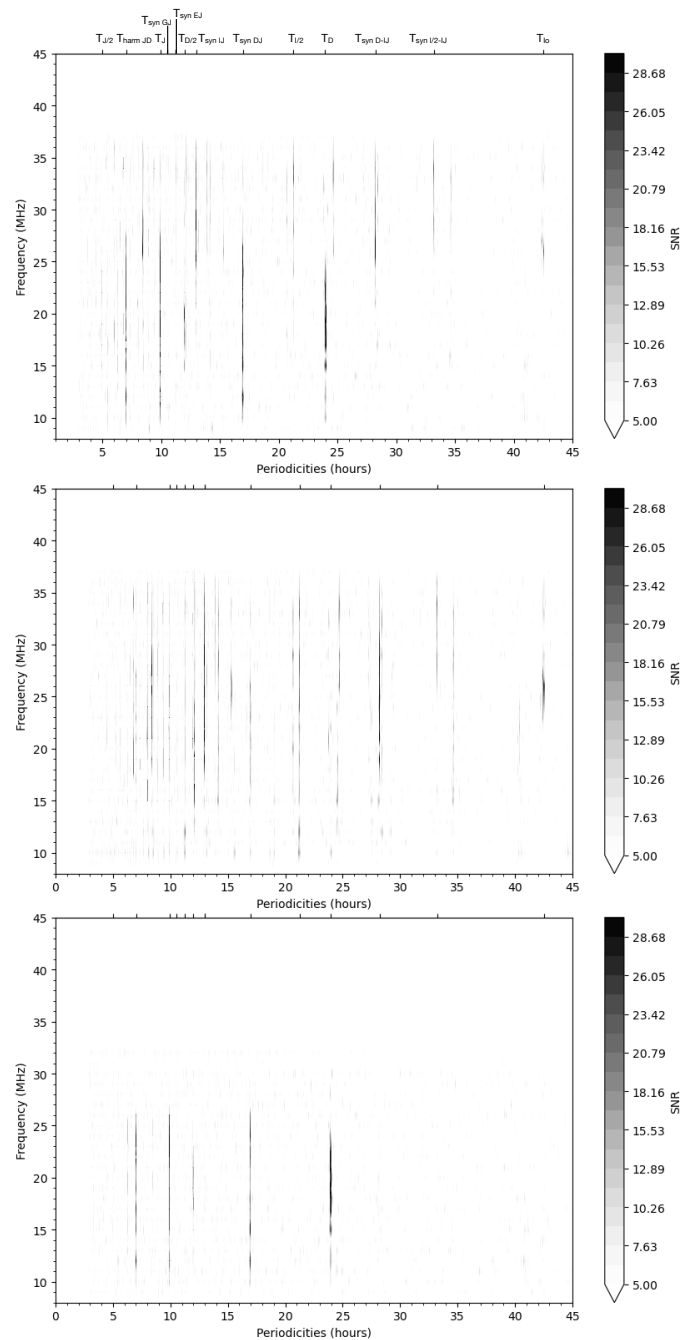


**Fig. A.1.** Signal to Noise ratio of the 2D Lomb–Scargle Periodogram for (top panel) All emissions, (middle panel) Io-induced emissions, (bottom panel) non-Io emissions. Y-axis represents the observed frequencies (from 8 to 45 MHz), X-axis represents the Lomb–Scargle Periodicities. Periodicities of interest are indicated above the top y-axis.

In this Appendix, we detail the results of our Lomb–Scargle analysis of the Marques et al. (2017a) Nançay Decameter Array Catalog, ranging from January 1990 to April 2020. In this catalog, all observed Jovian emissions, were labelled with respect to their time-frequency morphology, their dominant circular po-

larization and maximum frequency. They are separated between Io and non-Io induced radio emissions. Figure A.1 display the SNR of the 2D LS Periodograms for all emissions (top panel) and separated between Io-induced (middle panel) and non-Io emissions (bottom panel). For Io-induced emissions, high SNR are clearly visible at all periodicities related to Io ( $T_{Io}$ ,  $T_{Io/2}$ ,  $T_{syn Io/2-IJ}$ ,  $T_{syn D-IJ}$ ,  $T_{syn IJ}$ ). For Non-Io induced emissions, high SNR are visible for periodicities linked to either Jupiter ( $T_J$ ) or the day ( $T_D$ ,  $T_{D/2}$ ), or combination of both ( $T_{syn DJ}$ ,  $T_{harm DJ}$ ). These periodicities are detected at lower observed frequency (up to 26 MHz only) than Io-induced emission, due to magnetic field topology. No clear peak are visible for Europa and Ganymede, which is also not surprising at they are not that often visible in the data, even if there were statistically detected using this catalog (Zarka et al. 2017, 2018; Jácome et al. 2022), but after having being sorted by position of the moons as a function of the observer.